

Draft of October 4, 2018

Observations of T Tauri Disks at Sub-AU Radii: Implications for Magnetospheric Accretion and Planet Formation

J.A. Eisner¹, L.A. Hillenbrand¹, R.J. White¹, R.L. Akeson², & A.I. Sargent¹

jae@astro.caltech.edu

ABSTRACT

We determine inner disk sizes and temperatures for four solar-type (1-2 M_{\odot}) classical T Tauri stars (AS 207A, V2508 Oph, AS 205A, and PX Vul) using 2.2 μm observations from the Keck Interferometer. Nearly contemporaneous near-IR adaptive optics imaging photometry, optical photometry, and high-dispersion optical spectroscopy are used to distinguish contributions from the inner disks and central stars in the interferometric observations. In addition, the spectroscopic and photometric data provide estimates of stellar properties, mass accretion rates, and disk co-rotation radii. We model our interferometric and photometric data in the context of geometrically flat accretion disk models with inner holes, and flared disks with puffed-up inner walls. Models incorporating puffed-up inner disk walls generally provide better fits to the data, similar to previous results for higher-mass Herbig Ae stars. Our measured inner disk sizes are larger than disk truncation radii predicted by magnetospheric accretion models, with larger discrepancies for sources with higher mass accretion rates. We suggest that our measured sizes correspond to dust sublimation radii, and that optically-thin gaseous material may extend further inward to the magnetospheric truncation radii. Finally, our inner disk measurements constrain the location of terrestrial planet formation as well as potential mechanisms for halting giant planet migration.

Subject headings: stars:pre-main sequence—stars:circumstellar matter—stars:individual(AS 207, V2508 Oph, AS 205, PX Vul)—techniques:high angular resolution—techniques:interferometric

¹California Institute of Technology, Department of Astronomy MC 105-24, Pasadena, CA 91125

²California Institute of Technology, Michelson Science Center MC 100-22, Pasadena, CA 91125

1. Introduction

T Tauri stars are low-mass ($\lesssim 2 M_{\odot}$) pre-main sequence objects, thought to be early analogs of stars like our own Sun. A wealth of evidence, including direct imaging at millimeter and optical wavelengths (e.g., Koerner & Sargent 1995; Dutrey et al. 1996; McCaughrean & O’Dell 1996), and modeling of spectral energy distributions (SEDs; e.g., Adams et al. 1988; Bertout et al. 1988; Beckwith et al. 1990), has confirmed the long-espoused hypothesis that T Tauri stars are surrounded by massive disks of dust and gas. Moreover, observed line profiles and UV continuum excesses indicate that T Tauri stars are actively accreting material from their circumstellar disks (e.g., Walker 1972; Edwards et al. 1994; Gullbring et al. 1998).

The structure of the innermost disk regions may reveal the mechanism by which material is accreted through the disk onto the star. In the current paradigm, T Tauri disks are truncated by the stellar magnetosphere within the co-rotation radius, with material accreting along magnetic field lines onto high-latitude regions of the star (e.g., Königl 1991; Shu et al. 1994). For typical T Tauri star masses, radii, magnetic field strengths, and accretion rates, predicted truncation radii range from $\sim 0.02 - 0.2$ AU. Observational measurements of these truncation radii are an obviously important test of the theory of magnetospheric accretion.

The spatial and temperature structures of inner circumstellar disks are also important for understanding the properties of dust and gas in the terrestrial planet region, and ultimately for understanding the formation of planets. For example, a puffed-up inner disk wall, due to the normal angle of incidence of stellar radiation on the truncated inner edge (e.g., Dullemond et al. 2001), may lead to shadowing, and thus cooler temperatures in the inner disk compared to standard flat or flared disk temperature profiles (e.g., Chiang & Goldreich 1997). This, in turn, would have profound implications as to how and where terrestrial planets form (e.g., Hayashi 1981; Sasselov & Lecar 2000). Furthermore, inner disk structure is important for understanding how the close-in extra-solar planets discovered by radial velocity surveys (e.g., Marcy & Butler 2000) either formed at, or migrated to their observed orbital radii (e.g., Lin et al. 1996).

Currently, only near-IR interferometric observations have sufficient spatial resolution to probe directly the geometry and temperature of hot ($\sim 1000 - 2000$ K) disk regions within ~ 1 AU of young stars. Observations of the inner disks of a few of the brightest T Tauri stars (Akeson et al. 2000; Colavita et al. 2003) and of their more massive counterparts, Herbig Ae stars (Millan-Gabet et al. 1999, 2001; Eisner et al. 2003, 2004), demonstrated that inner disks around lower-mass stars ($\lesssim 5 M_{\odot}$) are larger than inferred by fitting geometrically thin accretion disk models to SEDs (e.g., Beckwith et al. 1990). Inclusion of puffed-up inner walls in the models leads to consistent fits to both interferometric and SED data for these

objects (Eisner et al. 2004; Muzerolle et al. 2003). On the other hand, higher-mass Herbig Be stars (Eisner et al. 2004) and the extreme accretor FU Ori (Malbet et al. 1998, 2005) are fitted well with simple flat disk models, suggesting that inner disk structure may depend on accretion rates or stellar properties. A larger sample of resolved inner disks, including lower-mass T Tauri stars, is necessary to explore such trends.

Here, we present 2.2 μm Keck Interferometer observations of the inner disks around four solar-type (1-2 M_{\odot}) T Tauri stars, potential analogs to our own young Sun. In order to model the stellar and circumstellar emission accurately, we combine our spatially resolved interferometry data with optical/near-IR SEDs and high-resolution echelle spectra. The photometric and spectroscopic data are essential for decomposition of the observed 2.2 μm flux into stellar and excess components. Since T Tauri stars are variable at near-IR wavelengths on timescales of several days to months (e.g., Skrutskie et al. 1996), our spectroscopic, photometric, and interferometric data were obtained within several days of one another. The photometry and spectra also enable determination of various properties of these systems, including stellar masses, ages, temperatures, radii, $v \sin i$, binarity, mass accretion rates, magnetospheric truncation radii, and co-rotation radii.

From the 2.2 μm interferometry data, we establish inner disk radii and temperatures, and distinguish between flat and puffed-up inner disk models. In addition, we compare these measured sizes with inferred magnetospheric and co-rotation radii. Although our sample is small, the range of stellar and accretion properties allows us to explore how inner disk structure depends on these parameters.

2. Observations and Data Reduction

2.1. Sample

Our sample consists of four classical T Tauri stars: AS 207A, V2508 Oph, AS 205A, and PX Vul. AS 207A, the optically-brightest T Tauri star in ρ Oph, was identified as a young star based on its $\text{H}\alpha$ emission (Struve & Rudkjøbing 1949), and also as one component of a $0''.6$ binary system (Ghez et al. 1993). The T Tauri star V2508 Oph (Walter 1986) is located near the L162 dark cloud. AS 205A is a well-known young star near the ν Sco dark nebula (e.g., Merrill & Burwell 1950), identified as the brightest component of a $1''.3$ binary system by Ghez et al. (1993). We assume that AS 207A, V2508 Oph, and AS 205A are all at the approximate distance of the ρ Oph cloud, 160 pc (Chini 1981). Finally, PX Vul is a T Tauri star in the Vul R2 region, at a distance of 420 pc (e.g., Herbig & Kameswara Rao 1972; Herbst et al. 1982). Properties of our sample, including celestial coordinates, distances, and

spectral types, are included in Table 1.

2.2. 2.2 μm Interferometry

We observed AS 207A, V2508 Oph, AS 205A, and PX Vul with the Keck Interferometer (KI) on June 2, 2004. KI is a fringe-tracking long baseline near-IR Michelson interferometer combining light from the two 10m Keck apertures (Colavita & Wizinowich 2003; Colavita et al. 2003). The fringe-tracker detects a source in a 5ms integration, setting a limiting K -band magnitude of $m_K \sim 9$. In addition, sources must be optically bright enough for the adaptive optics (AO) systems on each Keck aperture. Superb seeing ($\lesssim 0''.5$) allowed excellent AO performance for our sample.

For each target, we measured squared visibilities (V^2) at K -band ($\lambda_0 = 2.2 \mu\text{m}$, $\Delta\lambda = 0.4 \mu\text{m}$). The system visibility (i.e., the point source response of the interferometer), was measured using observations of unresolved calibrators, weighted by the internal scatter in the calibrator and the temporal and angular proximity to the target source (Boden et al. 1998). Source and calibrator data were corrected for detection biases as described by Colavita (1999) and averaged into 5s blocks. The calibrated V^2 for the target sources are the average of the 5s blocks in each integration, with uncertainties given by the quadrature addition of the internal scatter and the uncertainty in the system visibility. Typical uncertainties are $\sim 5\%$.

All calibrators were chosen to be compact (angular diameters $\lesssim 0.2 \text{ mas}$) and close to the target sources (within $\sim 10^\circ$). In addition, our calibrators have K -band magnitudes similar to those of our targets, to minimize potential biases. At optical wavelengths, the calibrators are brighter than the targets, which may lead to enhanced AO performance; by measuring the photon counts along both interferometer arms and applying a standard “ratio correction” (e.g., Colavita 1999), we calibrate out the effects of AO performance on the visibilities. The data for AS 207A, V2508 Oph, and AS 205A were calibrated using HD 142943 and HD 148968, and data for PX Vul were calibrated using HD 181383 and HD 182919.

2.3. JHK Adaptive Optics Imaging

We obtained dithered imaging observations of our sources at J , H , and K on June 4, 2004, using the Palomar 200-inch adaptive optics system (Troy et al. 2000) with the PHARO camera (Hayward et al. 2001). After bias correction, background subtraction, and flat-

fielding of the images, photometric fluxes were measured with respect to the same calibrators used in our KI observations. Calibrator magnitudes are known from the 2MASS catalog, assuming they are non-variable. The photometric errors are given by the quadrature addition of the RMS variations in brightness between source integrations and the uncertainties in the calibrator magnitudes. Since the sources and calibrators were observed at similar airmasses, we apply no atmospheric extinction corrections. The measured fluxes for these sources are listed in Table 2.

With the high angular resolution afforded by adaptive optics imaging ($\sim 0''.1$ at K -band) we were able to resolve AS 207 and AS 205 into binaries, finding parameters (see Table 3) consistent with previous measurements (Ghez et al. 1993; Reipurth & Zinnecker 1993; Koresko 2002; Barsony et al. 2003). For these systems, we measured photometric fluxes for both the primaries and secondaries; JHK magnitudes for the primaries are listed in Table 2, and ΔJHK values are given in Table 3. Since the projected binary separations are much larger than the field of view of KI (50 mas), we obtained interferometric data only for the primaries. No spatially resolved companions brighter than $\Delta K = 5$ were detected near V2508 Oph or PX Vul, and we consider these to be single stars hereafter.

2.4. *UBVRI* Photometry

We observed our sample through Johnson U, B, V , and Kron R and I filters on June 8, 2004 using the robotic Palomar 60-inch telescope. Photometric fluxes were measured from bias-corrected, flat-fielded images using well-studied photometric standards (Landolt 1992). We determined extinction corrections and magnitude zero-points using observations of five Landolt standards obtained throughout the night. Photometric errors for our target sources are the sum of various uncertainties in quadrature: the RMS variation between integrations (where multiple integrations of a source are available), the uncertainties in zero-points and extinction coefficients, and uncertainties in magnitudes of our calibrators. Photometric uncertainties are typically $\lesssim 10\%$, except at U -band, where substantial uncertainties in the extinction coefficients lead to large error bars for the measured fluxes.

The seeing-limited resolution of these observations was $\sim 1''.7$, and the close binaries in our sample, AS 207 and AS 205, are unresolved. Optical photometry for these sources, listed in Table 2, therefore includes contributions from both the primaries and the secondaries.

2.5. High Resolution Optical Spectroscopy

High dispersion optical spectra of the sample were obtained on 2004 June 11 using the HIRES spectrograph (Vogt et al. 1994) on Keck I. HIRES was used with the red collimator, an RG-610 filter, and the D1 decker ($1''.15 \times 14''.0$), yielding $R \approx 34,000$ spectra over 6330–8750 Å, with gaps between orders. An internal Quartz lamp and a ThAr lamp were observed with the same setup for flat fielding and dispersion correction. Several dwarf spectral type standards with known radial velocities were also observed to assist in the spectroscopic analysis. The binary AS 205 was observed with the slit along the axis of the pair, while AS 207 (an unresolved binary in these observations), V2508 Oph and PX Vul were observed with the slit perpendicular to the horizon (vertical mode).

The HIRES spectra were reduced using the facility “makee” reduction script written by Tom Barlow. Reduction includes bias-correction, flat-fielding, spectral extraction, sky subtraction, wavelength calibration, and heliocentric radial velocity corrections. This procedure worked well for single stars, but not for the components of AS 205 whose spectra overlap. In that case, the component spectra were determined by fitting two Gaussians to each one-dimensional cut in the spatial direction of the two-dimensional spectra. The FWHM of the best fit Gaussians were $0''.4$; the seeing was quite good and the $1''.2$ pair is reasonably well resolved. These extracted component spectra were then assigned the wavelength solution of the combined system as determined by makee. Portions of the extracted spectra for our sources are shown in Figure 1.

3. Analysis

Calibrated $2.2 \mu\text{m}$ KI visibilities (§2.2) and de-reddened SEDs (§§2.3–2.4) for our sample are shown in Figures 2–5. V^2 values are plotted as a function of $u - v$ radius, r_{uv} , and SEDs use units of λF_λ . The SEDs were constructed from our measured $UBVR IJHK$ photometry, corrected for binarity in the case of AS 207 and AS 205 (Table 3; §3.1.1), and de-reddened using the A_V values in Table 1. Figures 2–5 also include longer-wavelength ($> 3 \mu\text{m}$) photometry from the literature.

Measured $2.2 \mu\text{m}$ KI visibilities and broadband SEDs constrain the sizes and temperatures of inner disks around the observed sources. However, the near-IR stellar flux contribution to both the SEDs and visibilities must be removed before modeling the circumstellar component. We determine the stellar properties of our sample in §3.1.1 based on our spectroscopy and photometry, and use Kurucz models to determine stellar fluxes at near-IR wavelengths (see Figures 2–5; Table 4). Removing the stellar contributions, we are left with

the circumstellar components of the visibilities and SEDs.

We model these circumstellar components in terms of 1) a geometrically flat accretion disk and 2) a flared, two-layer, irradiated disk with a puffed-up inner wall (§3.3; as in Eisner et al. 2004). For each source, we compute a grid of models for varying inner disk sizes and temperatures, and find the “best-fit” model for which the χ^2 between the model and the data is minimized. SEDs and visibilities computed for the best-fit models are shown in Figures 2–5, and best-fit inner disk sizes and temperatures are listed in Table 5. Longer-wavelength photometry from the literature is used to qualitatively constrain disk flaring (§3.4), although it is not used in our disk model-fitting.

In order to compare our derived inner disk sizes with those expected from magnetospheric accretion theory, we use veiling values and shorter wavelength photometry to constrain mass accretion rates (§3.1.2) and thereby determine magnetospheric truncation radii (§3.1.3). Inferred $v \sin i$ values allow estimates of disk co-rotation radii (§3.1.4) for comparison purposes.

3.1. Stellar and Accretion Properties

3.1.1. Stellar Properties

We determined radial velocities, rotational velocities, spectral types, and continuum excesses for our sample from optical spectra (Table 1), following White & Hillenbrand (2004). Radial velocities and $v \sin i$ values are estimated by fitting a parabola to the peak of the cross-correlation functions, derived using dwarf stars of similar spectral type. The spectral types and the optical veiling levels at $\sim 6500 \text{ \AA}$ and $\sim 8400 \text{ \AA}$ (defined as $r_{R,I} = F_{\text{excess}}/F_{\text{photosphere}}$) are established simultaneously by comparisons with artificially veiled dwarf standards¹. For the binary AS 205, spectral types are determined for both components from spatially-resolved spectra. In this discussion, we focus on AS 205A, but analysis of AS 205B, itself resolved into a spectroscopic binary, is included in Appendix A. The binary AS 207 is spatially unresolved in the spectral data, preventing extraction of individual components. However, the large flux ratio for the AS 207 components (Table 3) suggests that the spectral type of the system is dominated by that of AS 207A. AS 207A, V2508 Oph, and AS 205A have mid-K spectral types, while PX Vul is hotter, with a spectral type of F3.

¹The lines used to measure spectral types and veilings are not gravity dependent, and thus dwarf standards are suitable even though they have higher surface gravities than our T Tauri sample (see White & Hillenbrand 2004, for further discussion).

Since the optical photometry does not resolve the components of AS 205 and AS 207 (§2.4), we measure flux ratios from adaptive optics or spectroscopic observations and use the spectral types for the components to determine flux ratios at wavelengths where the pairs are spatially unresolved. For AS 205, the two Gaussian fits to echelle spectra (§2.4) provide a direct measure of the flux ratios at R and I bands of 0.16 and 0.24, respectively. The independently determined spectral types then provide estimates of flux ratios for the spatially unresolved UBV measurements. For AS 207, the two components are unresolved in the echelle spectra and we employ a less direct procedure. We assume that the spatially-resolved J-band measurement (§2.3) probes the photosphere of each component, and then predict flux ratios at the shorter, spatially unresolved wavelengths using the measured spectral type for AS 207A (K5) and an assumed spectral type of M3 for the secondary. The companion’s spectral type is consistent with both the observed J-band flux ratio and the cooler spectral types assigned from near-infrared spectroscopy and photometry for the composite system (Doppmann et al. 2003; Geoffroy & Monin 2001).

Stellar temperatures are assigned based on measured spectral types assuming a dwarf temperature/spectral type relation (e.g., Hillenbrand & White 2004). Extinctions and stellar luminosities are determined by comparing the veiling-corrected $R-I$ fluxes to those expected from Kurucz models most similar in temperature, assuming $\log g = 4$ (appropriate for pre-main sequence stars aged 1-10 Myr; e.g., Piorno Schiavon et al. 1995), the extinction relation of Steenman & Thé (1991), and the distances listed in Table 1. Stellar radii are estimated from the luminosities and temperatures using the Stefan-Boltzmann equation. Temperatures, luminosities, radii, and extinctions for these stars are listed in Table 4. We estimate that the assumed stellar temperatures are accurate to ± 100 K, while luminosities, radii, and extinction estimates are uncertain by $\sim 20 - 30\%$.

Stellar masses and ages are estimated by comparing the luminosities and temperatures with the predictions of pre-main sequence evolutionary models (Siess et al. 2000)². These comparisons lead to masses near $1 M_{\odot}$ for the 3 K-type stars, and $2.0 M_{\odot}$ for the F3 star. Stellar ages range from 0.6 to 6.9 Myr (Table 4). While considerable uncertainties in pre-main sequence evolutionary models may lead to large errors in absolute ages, the relative ages are more secure. Including adopted uncertainties of 100 K for stellar temperature and 30% for stellar luminosity, AS 207A and V2508 Oph appear to be the youngest stars in the sample, while AS 205A is somewhat older, and PX Vul is older still. We note that the apparent spread in ages may also correspond to different accretion histories for different

²We prefer evolutionary models of Siess et al. (2000) because they span a larger range of stellar masses than those of Baraffe et al. (1998), and are more consistent with measured dynamical masses than D’Antona & Mazzitelli (1997) models.

sources, which could lead to variations in the birthline for pre-main sequence models; thus, the relative ages should be treated with some caution.

3.1.2. Mass Accretion Rates

Relative accretion rates for our sample are constrained qualitatively by H α emission lines in our spectra (Figure 1). Equivalent widths of H α and full-widths at 10% of the peak are listed in Table 1. These strong, broad profiles suggest on-going accretion in all sources (e.g., White & Basri 2003), with relatively smaller accretion rates for AS 207A and V2508 Oph.

Quantitative estimates of mass accretion rates are calculated from the accretion luminosity generated by infalling material (Gullbring et al. 1998):

$$\dot{M} = \frac{L_{\text{acc}} R_*}{GM_*(1 - R_*/R_{\text{inner}})}. \quad (1)$$

Here, L_{acc} is the accretion luminosity, R_* is the stellar radius, M_* is the stellar mass, and R_{inner} is the inner disk radius. We adopt values of R_{inner} from Table 5 (using puffed-up inner disk sizes determined from combined V^2 +SED analysis; see §3.3); these are inner radii of the dust disks, and may be somewhat larger than the inner gas radii relevant for this formula (as discussed in §5.2), which would consequently lead to larger inferred mass accretion rates.

The accretion luminosity, L_{acc} , is estimated by applying a bolometric correction factor to a flux excess measured over a limited wavelength range. We calculate accretion luminosities using two methods, one based on measured veiling at R -band (e.g., Hartigan & Kenyon 2003; White & Hillenbrand 2004), and the other based on measured U -band excess emission (Gullbring et al. 1998). For the first method, R -band excess luminosities are calculated from the measured veilings and then converted into accretion luminosities using a bolometric correction of 35. The bolometric correction factor is highly uncertain, and probably introduces uncertainties of a factor of ~ 3 in the computed accretion luminosities. We also calculate the accretion luminosity from the observed U -band excess luminosity (L_U) following Gullbring et al. (1998):

$$\log(L_{\text{acc}}/L_{\odot}) = 1.09_{-0.18}^{+0.04} \log(L_U/L_{\odot}) + 0.98_{-0.07}^{+0.02}. \quad (2)$$

Although the accretion luminosities calculated using Equation 2 use a smaller bolometric correction than for the first method (due to the assumed high temperature of the accretion excess; Calvet & Gullbring 1998), the large photometric uncertainties for our U -band data (Table 2) introduce errors of a factor of ~ 2 . We find that accretion estimates based on U -band fluxes are typically higher than those computed from R -band measurements, although

the two estimates are consistent to within a factor of 2. Since the accretion luminosities estimated from both methods have large error bars, we adopt the mean of the two values in our analysis. Inferred accretion luminosities for our sample range from $0.4 L_{\odot}$ to $25.0 L_{\odot}$, and are listed in Table 4.

Using these adopted values for L_{acc} , we calculate mass accretion rates from Equation 1. For our sample, \dot{M} is between $3.2 \times 10^{-8} M_{\odot} \text{ yr}^{-1}$ and $1.3 \times 10^{-6} M_{\odot} \text{ yr}^{-1}$ (Table 4). The large uncertainties for L_{acc} lead to accretion rates that are probably uncertain by a factor of 2-3.

3.1.3. Magnetospheric Radii

The expected radius of magnetospheric truncation, R_{mag} , is determined by the balance of forces between infalling (accreting) material and the stellar dipole field (Königl 1991):

$$\frac{R_{\text{mag}}}{R_*} = 2.27 \left[\frac{(B_0/1 \text{ kG})^4 (R_*/R_{\odot})^5}{(M_*/M_{\odot})(\dot{M}/10^{-7} M_{\odot} \text{ yr}^{-1})^2} \right]^{1/7}. \quad (3)$$

With the stellar parameters determined in §3.1.1, the accretion rates calculated in §3.1.2, and assuming a typical magnetic field strength for T Tauri stars of 2 kG (Johns-Krull et al. 2003), we calculate R_{mag} for our sample. Our values for R_{mag} range from 0.03 to 0.13 AU (Table 4). Propagating the assumed uncertainties for R_* , M_* , and \dot{M} , and adopting an uncertainty of 30% for B_0 , we estimate that the magnetospheric radii are uncertain by $\sim 30\%$.

3.1.4. Co-Rotation Radii

The co-rotation radius is the radius at which the Keplerian orbital period in the disk equals the stellar rotation period. We derive co-rotation radii for stars with $v \sin i$ measurements (Table 1) according to:

$$R_{\text{co-rotation}} = (GM_*)^{1/3} \left(\frac{R_*}{v} \right)^{2/3} \leq (GM_*)^{1/3} \left(\frac{R_*}{v \sin i} \right)^{2/3}. \quad (4)$$

Here, M_* is the stellar mass, R_* is the stellar radius, $v \sin i$ is the projected rotational velocity of the star, and i is the inclination of the system. For AS 207A, where there is a reported photometric period, $\tau = 6.53$ days (Shevchenko & Herbst 1998; Bouvier 1990), the inclination (and hence the co-rotation radius) can be determined explicitly. For the remaining sources, without known rotation periods (Shevchenko & Herbst 1998), we derive

upper limits. Co-rotation radii and upper limits range from 0.03 to 0.09 AU, and are listed in Table 4. Propagating the uncertainties in M_* , R_* , and $v \sin i$ (assuming stellar mass and radius are uncertain by $\sim 30\%$), we estimate that the derived co-rotation radii are uncertain by approximately 20%.

3.2. Near-IR Stellar and Excess Fluxes

The measured 2.2 μm visibilities and near-IR SEDs contain information about inner circumstellar disks as well as the central stars, and distinguishing the stellar and excess fluxes is crucial to accurate modeling of the disks. Because the stellar SED peaks closer to 2.2 μm for our current sample than for the hotter stars analyzed in Eisner et al. (2004), this step is especially critical here. In this Section, we discuss our procedure for removing the stellar component from the V^2 and SED data, and in §3.3, we model the circumstellar component and determine disk parameters.

The measured SED at near-IR wavelengths is simply the sum of the stellar and disk fluxes. Our 2.2 μm visibilities are given by

$$V_{\text{meas}}^2 = \left(\frac{F_* V_* + F_{\text{D}} V_{\text{D}}}{F_* + F_{\text{D}}} \right)^2 \approx \left(\frac{F_* + F_{\text{D}} V_{\text{D}}}{F_* + F_{\text{D}}} \right)^2, \quad (5)$$

where F_* is the stellar flux, $V_* \approx 1$ are the visibilities due to the unresolved central star, F_{D} is the circumstellar disk flux, and V_{D} are the visibilities due to the disk. A knowledge of the stellar flux at near-IR wavelengths is critical for modeling the circumstellar components of both the 2.2 μm visibilities and the near-IR SEDs. This flux can be estimated using the stellar parameters from §3.1.1 and extrapolating the veiling-corrected flux measured at optical wavelengths using a Kurucz model. The excess 2.2 μm flux due to the compact circumstellar disk is the difference between the de-reddened observed flux and the Kurucz model. These 2.2 μm stellar and excess fluxes are listed in Table 4.

The inferred stellar and excess fluxes are somewhat uncertain, leading to uncertainties in the derived disk parameters. For AS 205A and PX Vul, where the excess flux dominates the emission, uncertainties in the relative fluxes will have a small effect on disk parameters. However, when the stellar and excess fluxes are comparable, as for AS 207A and V2508 Oph, there can be significant errors in the fitted disk sizes. For example, 30% errors in 2.2 μm stellar flux lead to size errors of 25% and 23% for AS 207A and V2508 Oph, but only 2% and 7% for AS 205A and PX Vul.

In addition to the central star and circumstellar disk, there may be other contributions to the visibilities and SEDs. Emission on scales between the ~ 5 mas KI fringe spacing and

the ~ 50 mas field of view, for example, due to thermal or scattered emission from residual envelopes, will be resolved out and will lower the overall measured visibilities and lead to larger inferred sizes. If the extended emission has a similar spectrum to the star, as expected for scattering from large dust grains, it will not affect the SED. Extended emission is difficult to constrain, since observations that can resolve faint emission on angular scales smaller than 50 mas are virtually non-existent. However, previous analysis of the visibilities and SEDs of more luminous Herbig Ae/Be stars indicates small ($\lesssim 1\%$) contributions from extended emission on $\lesssim 1''$ scales (Eisner et al. 2004). For KI, which has a field of view of only 50 mas, we expect the contribution from extended emission for our less luminous T Tauri star sample to be even smaller.

Near-IR emission may also arise from hot gas in accretion shocks at the stellar photosphere (e.g., Calvet & Gullbring 1998; Gullbring et al. 2000), or hot optically thin gas in the inner disk (interior to the dust truncation radius; e.g., Akeson et al. 2005). Since these hot gas components are compact compared to emission from the circumstellar dust disk, they would tend to raise the visibilities compared to those predicted by our Equation 5; i.e., lead to smaller inferred disk sizes. In contrast, for the measured SEDs hot gas would contribute extra emission, leading to *larger* inferred disk sizes. We expect that the fraction of near-IR emission from an 8000 K accretion shock (Calvet & Gullbring 1998) will be relatively small compared to peak emission from a 1000-2000 K disk. However, emission from hot gas may cause a measurable effect on the 2.2 μm visibilities and near-IR SEDs for sources with extremely high accretion rates (see §4.3).

In the analysis below, we assume that near-IR emission from extended dust or hot gas is insignificant compared to the stellar and disk emission. Thus, we model the SED using a Kurucz stellar atmosphere plus thermal emission from a disk, and use Equation 5 to model the measured visibilities.

3.3. Modeling Inner Disk Structure

Equipped with the stellar and circumstellar contributions to the visibilities and SEDs (§3.2), we fit the circumstellar components using the two simple disk models described in detail by Eisner et al. (2003, 2004): 1) a geometrically flat accretion disk with a temperature profile $T(R) \propto R^{-3/4}$ (Lynden-Bell & Pringle 1974), truncated at an inner radius, R_{in} ; and 2) a flared, irradiated, two-layer disk (Chiang & Goldreich 1997) incorporating a puffed-up inner disk wall at R_{in} (Dullemond et al. 2001). The main difference between the two models is the angle of incidence of stellar radiation: for the flat disk, stellar radiation is incident at glancing angles, while the puffed-up inner disk and flared outer surface intercept

starlight at more normal angles, leading to additional disk heating. For the second model, the near-IR emission is dominated by the puffed-up inner rim, and the emission appears essentially ring-like at the $2.2 \mu\text{m}$ wavelength of our interferometric observations. While the geometrically-thin disk model assumes blackbody emission, we assume the opacity for the puffed-up inner disk model is due to astronomical silicate dust (Draine & Lee 1984).

For each model, the parameters relevant for the inner disk structure are the inner radius, R_{in} , and the temperature of the disk at the inner radius, T_{in} . Temperatures at other disk radii are specified by these parameters and the assumed temperature profiles for the disk models. The V^2 and SED data (and associated error bars) used in the modeling are shown in Figures 2-5. We use only *RIJHK* photometry, and de-veil the *RI* fluxes, so that the data traces only the inner disk, uncontaminated by hot accretion excess emission which can dominate at shorter wavelengths.

With the limited amount of data available (2-4 visibilities, and 5 photometric points for each source), we consider only face-on disk models here. As discussed in Eisner et al. (2004), including inclination in the models may affect the results. Unless the baseline position angle corresponds with the major axis of an inclined disk, the size inferred from V^2 measurements for a face-on model would be underestimated with respect to the inferred size for an inclined model. Similarly, the face-on assumption would lead to an underestimate of disk size from SED data, since a face-on disk produces more near-IR flux than an inclined disk of the same size. Further interferometric observations, probing a range of position angles, are necessary to constrain the parameters of inclined disk models. However, assuming our sources are not close to edge-on (reasonable given that the central stars are un-obscured), inclination effects will not substantially alter the results presented here for face-on disk models.

We fit our $2.2 \mu\text{m}$ KI visibilities and SED data simultaneously and determine the best-fit parameter values, R_{in} and T_{in} , by calculating χ^2 for models over a grid of inner radii and temperatures. In practice, we fit for the directly observable angular (rather than linear) size of the inner radius, θ_{in} ; best-fit values are converted to linear sizes using the distances in Table 1. We consider θ_{in} ranging from 0.1 to 10 mas in increments of 0.01 mas (spanning the approximate angular resolution of KI), and T_{in} ranging from 1000 to 2500 K in 100 K increments (bracketing values expected for dust sublimation; e.g., Salpeter 1977; Pollack et al. 1994). For each model, we calculate the χ^2 of the combined V^2 +SED dataset, where each data point is weighted by its measurement uncertainty, and we find the inner disk size and temperature for which χ^2 is minimized. $1-\sigma$ uncertainties on the best-fit parameters are determined in the standard way (e.g., Eisner et al. 2004). Best-fit parameters, $1-\sigma$ uncertainties, and reduced χ^2 values are listed in Table 5. Puffed-up inner disk models generally provide small χ^2 values (indicating good fits to the data), with inner disk sizes and

temperatures ranging from 0.12 to 0.32 AU and 1000 to 1800 K, respectively. In contrast, flat disk models fit the data poorly, and suggest smaller inner disk sizes (0.02-0.22 AU) and higher temperatures (1400-2400 K).

The poor fits of flat disk models to the data are consistent with previous observations which showed that sizes determined from near-IR interferometry are often larger than those determined from SED modeling (e.g., Akeson et al. 2000; Millan-Gabet et al. 2001; Eisner et al. 2003). We investigate this issue here by fitting the visibility and SED data separately. For the SEDs, we use the same procedure and parameter grid as for the combined analysis. For the visibilities, where we have fewer data points, we fit only for θ_{in} , assuming the value of T_{in} determined from the combined analysis. The best-fit parameter values, uncertainties, and reduced χ^2 values are included in Table 5. We note that for the small numbers of visibility measurements, the reduced χ^2 are often very small, indicating poor constraints on the models. The results indicate that the V^2 or SED data individually can be fit reasonably well with either model, although the puffed-up inner disk model provides somewhat lower χ^2 values for the SED fits. For most sources, the inner size for flat disk models inferred from the visibilities is ≥ 5 times larger than inferred from the SEDs. The puffed-up inner disk models, in contrast, find best-fit sizes from the V^2 or SEDs generally consistent within the 1σ uncertainties (Table 5).

From the SEDs alone, we cannot distinguish between flat and puffed-up inner disk models, but combined V^2 +SED analysis shows that puffed-up inner disk models are preferred (Table 5). Qualitatively, this additional constraint comes from the spatially resolved information contained in the V^2 data. While near-IR SEDs constrain both the temperature and size of the inner disk, these parameters are degenerate with the spatial and temperature profiles, and thus SED fits are not unique; one can find a suitable fit for either the geometrically thin or puffed-up inner disk models by varying T_{in} and R_{in} . Combining SEDs with even a limited amount of interferometric data, we can measure *directly* the size of the inner disk, thereby breaking the degeneracy inherent in SED-only modeling and enabling us to distinguish between puffed-up and geometrically flat inner disk models.

The measured sizes discussed above are determined directly from the data. Since we separated the circumstellar components of the visibilities and SEDs from the stellar contributions in §3.2, the measured disk sizes do not depend on stellar properties or disk accretion rates; i.e., R_{in} and T_{in} are chosen simply to provide the best fit to the observations. Thus, the inner disk structure for our best-fit models is fully specified by R_{in} , T_{in} , and the assumed temperature profiles. Below, we investigate whether the stellar and accretion luminosities in these sources can provide sufficient disk heating to match the measured inner radii and temperatures, providing an additional test of whether the measured sizes are consistent with

the physical models.

For flat disk models, the expected temperature in the disk at 1 AU depends on heating by both stellar radiation and viscous dissipation of accretion energy (Lynden-Bell & Pringle 1974),

$$T_{1\text{AU}} = \left[2.52 \times 10^{-8} \left(\frac{R_*}{R_\odot} \right)^3 T_*^4 + 5.27 \times 10^{10} \left(\frac{M_*}{M_\odot} \right) \left(\frac{\dot{M}}{10^{-5} M_\odot \text{ yr}^{-1}} \right) \right]^{1/4}. \quad (6)$$

Thus, the expected disk temperature depends on T_* , R_* , M_* , and \dot{M} . Using the value of $T_{1\text{AU}}$ computed for our inferred stellar and accretion parameters (§3.1), we predict the radius in the disk where $T = T_{\text{in}}$ (where T_{in} is determined from combined V^2 +SED analysis),

$$\frac{R_{\text{flat}}}{\text{AU}} = \left(\frac{T_{1\text{AU}}}{T_{\text{in}}} \right)^{4/3}. \quad (7)$$

For the passive disk model with a puffed-up inner wall, the expected radius where $T = T_{\text{in}}$ depends on the total luminosity incident on the inner disk,

$$R_{\text{puffed-up}} = \sqrt{\frac{L_* + L_{\text{acc}}}{4\pi\sigma T_{\text{in}}^4} (1 + f)}. \quad (8)$$

Here, f is the ratio of the inner disk width to the inner radius, which we have assumed to be 0.10 (Dullemond et al. 2001). Equation 8 includes the effects of accretion luminosity, L_{acc} , in addition to the stellar luminosity (Muzerolle et al. 2003).

Expected inner radii for the two models, with and without accretion heating, are listed in Table 6. We compare these predictions with our measured sizes: for the puffed-up inner disk model, we use sizes measured from V^2 +SED data, while for the flat disk model, which provides poor fits to combined datasets, we use the inner disk sizes measured from V^2 -only data. Measured inner disk sizes are roughly consistent with expectations for puffed-up inner disk models based on the stellar parameters determined in §3.1.1. Moreover, for the high-accretion rate source AS 205A, the predicted size is more consistent with the measured size when accretion luminosity is included, demonstrating the importance of accretion in the disk structure for this object. In contrast, for AS 207A, V2508 Oph, and PX Vul, the predicted sizes of puffed-up inner disk models with $\dot{M} = 0$ are compatible with the measured sizes (Table 6), suggesting that stellar irradiation is the dominant effect in puffing up the inner disk edges. Expected sizes for the flat disk model are smaller than measured values for all sources except AS 205A. These results are compatible with the fact that the puffed-up inner disk models generally fit the visibility and SED data better than the flat disk models.

The best-fit inner disk sizes (Table 5) are larger than both the magnetospheric and co-rotation radii calculated in §3.1 (Table 4). We illustrate this graphically in Figure 6, where we plot the $2.2 \mu\text{m}$ brightness distributions for our best-fit puffed-up inner disk models, and indicate the positions of magnetospheric and co-rotation radii with dotted and dashed lines, respectively. The discrepancy between measured sizes and magnetospheric/co-rotation radii is relatively small for some sources ($\lesssim 2$), and large for others (> 5). The magnitude of these discrepancies depends to some extent on our assumptions. However, more realistic models including inclined disks and potentially lower stellar magnetic fields would actually exacerbate the differences between measured sizes and magnetospheric radii (magnetic fields substantially higher than the assumed 2 kG are unlikely; Johns-Krull et al. 2003).

3.4. Large-Scale Disk Structure

In §3.3, we modeled our *RIJHK* photometry and $2.2 \mu\text{m}$ visibilities, and determined inner disk radii and temperatures for our sample. These values of R_{in} , T_{in} also provide the normalization of the temperature profiles (for our two simple models) in the outer disk regions. Here, we combine our measurements and modeling of the inner disk with longer-wavelength photometry (3-100 μm ; Weaver & Jones 1992; Jensen & Mathieu 1997; Prato et al. 2003; Koresko 2002) which probes larger disk radii. Due to source variability and multiple sources within the large IRAS beam (as seen in 2MASS images), the uncertainties in this long-wavelength photometry are likely $\gtrsim 10\%$. Despite these uncertainties, the long-wavelength fluxes still yield rough constraints on outer disk structure.

We quantify disk flaring by how the height of the disk increases with radius: $H/R \propto R^\xi$. For a flat disk, $\xi = -1$, while for a fully flared disk in hydrostatic equilibrium, $\xi = 2/7$ (Chiang & Goldreich 1997). These two extremes correspond to the flat and puffed-up disk models used above. However, dust settling and/or grain growth could result in other values for ξ (Dullemond & Dominik 2004a,b). Here, we also consider the case of a somewhat, but not fully, flared disk with $\xi = 1/10$. Comparison of the un-flared, somewhat flared, and fully flared models with the data give a qualitative measure of the degree of flaring. Inclination effects, which are not included in our face-on models, will also suppress the long-wavelength flux (due to the smaller projected surface area), mimicking the effects of flatter disks. Thus, we do not attempt to determine ξ exactly, instead maintaining a qualitative approach.

The outer disk geometry, as illustrated by the long-wavelength photometry, seems to vary from source to source (Figures 2–5). In some sources (AS 207A, PX Vul), flatter outer disks are consistent with the data, while other objects (V2508 Oph, AS 205A) require significant outer disk flaring to explain the data.

4. Results for Individual Sources

Figures 2–5 show the flat (solid lines) and puffed-up (dotted lines) disk models that provide the best fits to combined V^2 +SED datasets. For each source see Table 5 for best-fit R_{in} , T_{in} , and reduced χ^2 values of these models. In general, puffed-up inner disk models with inner temperatures ranging from 1000-1800 K provide good fits to the data, while flat disk models provide poor fits to the SED and V^2 data.

4.1. AS 207A

AS 207A shows a weak near-IR excess and a mass accretion rate lower than other sources in our sample. The visibility and SED data are more consistent with the predictions of a cooler, puffed-up inner disk model than with a flat disk model ($\chi_r^2 = 0.21$ versus 1.07; Figure 2). Best-fit inner disk sizes and temperatures are ~ 0.25 AU and 1000 K for the puffed-up inner disk model. This size is approximately two times larger than the calculated magnetospheric and co-rotation radii (Figure 6).

The IRAS photometry for AS 207A is compatible with flat outer disk models. Although AS 207A has a binary companion, the steeply increasing flux ratio across J, H , and K (Table 3) suggests that the companion contributes little to the long-wavelength flux.

4.2. V2508 Oph

For V2508 Oph, a source with a relatively small accretion rate, the puffed-up disk model provides a better fit to our V^2 and SED data than the flat disk model ($\chi_r^2 = 0.98$, compared with 1.41). While the puffed-up inner disk size determined from the visibilities (0.20 AU) is somewhat larger than that determined from the SED (0.07 AU), the discrepancy has $< 1\sigma$ significance, and the fit to the combined V^2 +SED dataset produces a reasonable χ_r^2 value (Figure 3; Table 5). Furthermore, the measured inner disk size agrees well with (but is slightly larger than) the magnetospheric truncation radius calculated in §3.1.3 and the upper limit on co-rotation radius determined in §3.1.4 (Figure 6). The long-wavelength photometry is compatible with an outer disk that is somewhat flared ($\xi \sim 1/10$).

4.3. AS 205A

Fits to the combined V^2 +SED dataset have $\chi^2 \sim 4 - 6$, mainly due to the poor fit to the SED data. The flat accretion disk model provides a better fit to the combined V^2 +SED dataset than the puffed-up inner disk model, but both fits are of poor quality so it is difficult to distinguish between them. The best-fit inner disk sizes range from 0.07 to 0.14 AU, and inner disk temperatures are ~ 1900 K. These fitted inner disk sizes are significantly larger than the magnetospheric truncation radius computed in §3.1.3 and the upper limit on co-rotation radius calculated in §3.1.4 (Figure 6).

We suggest that the poor fits to the SED data for this source ($\chi_r^2 \gg 1$; Table 5) are due to near-IR emission from an accretion shock, which has not been included in our simple models. As discussed in §3.2, sources with very high accretion rates may produce substantial near-IR emission from hot accretion shocks; this hot, compact emission would lead to larger inferred sizes from the SED but smaller inferred sizes from the V^2 measurements. This is consistent with our results for the accretion-dominated source AS 205A ($L_{\text{acc}}/L_{\text{star}} \sim 10$), the only object in our sample for which model fits to the SED predict larger sizes than fits to the visibilities.

Neither the flat disk model nor the flared, puffed-up inner disk model reproduces the far-IR emission well. For the flat disk model, this discrepancy is most likely due to disk flaring, which is ignored in the model. While the flared disk model fits better, the measured 3-5 μm fluxes are substantially larger than predicted by the model. Given the extremely high inferred accretion rate for AS 205A, we suggest that viscous dissipation of accretion energy may lead to disk-heating, and thus additional puffing that is not included in the model.

4.4. PX Vul

The puffed-up inner disk model provides a good fit to the SED and visibility data for PX Vul ($\chi_r^2 = 1.09$). In contrast, the flat disk model provides a relatively poor fit to the combined dataset ($\chi_r^2 = 3.10$; Figure 5). The best-fit size and temperature for the puffed-up inner disk model are ~ 0.32 AU and 1500 K. Similar to AS 205A, this source has a high mass accretion rate and displays substantial hot excess emission from an accretion shock. However, the ratio of accretion to stellar luminosity is only ~ 2 for PX Vul, and there seems to be little near-IR emission due to this hot excess; the SED is therefore fit well by our best-fit disk model. The magnetospheric truncation radius and the co-rotation radius determined for PX Vul (Table 4) are substantially smaller than the measured inner disk size. Comparison of the IRAS photometry with our models suggests that the outer disk may be

moderately flared ($\xi < 1/10$).

5. Discussion

5.1. Emerging Properties of Inner Disks around T Tauri Stars

Inner sizes and temperatures of circumstellar disks around young stars have traditionally been determined by fitting disk models to SEDs (e.g., Beckwith et al. 1990; Hillenbrand et al. 1992; D’Alessio et al. 1999). However, recent interferometric observations of high-mass T Tauri and Herbig Ae/Be stars have shown that inner disks are often much larger than predicted by these SED models (Monnier & Millan-Gabet 2002; Eisner et al. 2004). Our new results presented in §4 confirm this trend for lower-mass T Tauri stars.

For AS 207A, V2508 Oph, and PX Vul, simple flat accretion disk models suggest much smaller sizes (when fit to SEDs) than those determined interferometrically. Models incorporating puffed-up inner walls and flared outer disks provide better fits to our V^2 and SED data than the simple flat disk models. This is consistent with previous studies of more massive Herbig Ae stars (Eisner et al. 2004; Leinert et al. 2004), and suggests that truncated disks with puffed-up inner walls describe lower-mass T Tauri stars in addition to more massive objects.

The one source in our sample for which the observed V^2 and SED values may be consistent with a simple flat accretion disk model is AS 205A, the object with the highest ratio of accretion to stellar luminosity. Recent observations of another accretion-dominated source, FU Ori, have shown a flat disk model to be appropriate (Malbet et al. 2005). Thus, the vertical structure of the inner disk may depend on the relative magnitude of stellar and accretion luminosities. However, as discussed in §4.3, a more complicated model that accounts for near-IR emission from accretion shocks is probably necessary to accurately fit the data for AS 205A, and we cannot rule out a puffed-up inner disk with our current analysis.

5.2. Dust Sublimation and Magnetospheric Truncation

The truncated disks around T Tauri and Herbig Ae stars may be explained by dust sublimation, which depends on the disk temperature and dust grain properties. An alternative truncation mechanism is magnetospheric disruption of the disk, which is expected to yield a range of inner disk truncation radii and temperatures depending on accretion rates and stellar magnetic fields (e.g., Kenyon et al. 1996). In reality, both mechanisms may be

operative in T Tauri disks: optically-thick dust disks (which produce most of the observed near-IR emission) may be truncated by dust sublimation, while an optically-thin ionized gas component may be truncated closer to the star by the stellar magnetic field.

The calculated magnetospheric radii (§3.1.3; Table 4) are smaller than the puffed-up inner dust disk radii measured from the visibilities and SEDs (Table 5) for all sources in our sample, suggesting that magnetospheric truncation is not a viable mechanism for truncating the dust disks in our sample. Stronger magnetic fields are an unlikely way to reconcile these differences, especially for AS 205A and PX Vul, where $|\vec{B}_*| > 20$ kG would be required to bring the magnetospheric truncation radii into agreement with the measured sizes. Assuming that accreting disk material travels to R_{mag} in the midplane before being funneled along magnetic field lines onto the star, the fact that $R_{\text{in}} > R_{\text{mag}}$ for all sources suggests that the gaseous component of these disks extends further inward than the dust.

We speculate that dust disks are truncated by sublimation while gaseous material in the disk midplane extends all the way to R_{mag} . The smaller discrepancies between R_{in} and R_{mag} for sources with lower accretion rates (Figure 6) are consistent with this scenario: accretional heating pushes the sublimation radius outward (Equation 8), leading to a larger measured inner dust disk size, while increased pressure from accreting material compresses the magnetospheric radius (Equation 3). For AS 207A and V2508 Oph, smaller accretion rates lead to magnetospheric truncation closer to the sublimation radii, consistent with the data. In contrast, the high accretion rates in AS 205A and PX Vul may lead to large dust sublimation radii and small magnetospheric radii, which could explain the larger differences between R_{in} and R_{mag} in these sources.

Under standard models of magnetospheric accretion, it is expected that $R_{\text{mag}} \lesssim R_{\text{corot}}$, since outside of co-rotation, the centrifugal barrier would prevent accretion of material above the disk midplane (Ghosh & Lamb 1979a,b; Kenyon et al. 1996; Shu et al. 1997). Moreover, the slow rotational velocities of T Tauri stars (compared to expectations for the collapse of rotating clouds; e.g., Hartmann & Stauffer 1989) are often explained by magnetic locking of the stellar rotation to the inner disk, which requires $R_{\text{mag}} \approx R_{\text{corot}}$ (e.g., Königl 1991; Shu et al. 1994). Figure 6 shows that our results are compatible with these models: $R_{\text{mag}} \approx R_{\text{corot}}$ for our sample. Although for V2508 Oph and AS 207A, the calculated (upper limits) on co-rotation radii are somewhat smaller than R_{mag} , the estimates agree within adopted uncertainties. Thus, our results are consistent with magnetospheric truncation of the gaseous component of circumstellar disks, and magnetic locking of the stellar rotation and the inner (gaseous) disk edge.

5.3. Implications for Planet Formation

Our results indicate that dust disks around T Tauri stars are truncated within 0.1 – 0.3 AU of the central stars. Since dust particles provide the building blocks for planetesimals, and ultimately planets, planet formation in these systems is unlikely interior to ~ 0.1 AU. However, our observations indicate that there *is* dust in the terrestrial planet forming region (i.e., $\lesssim 1$ AU). While our best-fit flat inner disk models predict temperatures near 1 AU between 280 and 500 K (Equation 7), too hot for ice condensation (e.g., Hayashi 1981), the puffed-up inner disk edges indicated by our data may cast a shadow over inner disk regions (e.g., Dullemond et al. 2001), leading to lower temperatures. Thus, the snowline may be located at smaller radii than predicted by flat inner disk models (e.g., Hayashi 1981; Sasselov & Lecar 2000). The location of the snowline has profound implications for the formation of planets, and snowlines at smaller radii may increase the efficiency of Earth-like planet formation (e.g., Raymond et al. 2004).

Inner disk truncation provides a natural mechanism for halting planetary migration (e.g., Lin et al. 1996), and may therefore be linked with the observed period distribution of close-in extra-solar planets. Specifically, one expects migration to cease in a 2:1 resonance with the inner disk radius, corresponding to $0.63R_{\text{in}}$ (Lin et al. 1996). Kuchner & Lecar (2002) argue that the disk density may drop precipitously within the dust sublimation radius, and that it is therefore the dust truncation radius that is important for halting migration. For the measured inner dust radii of our sources, migrating planets would be halted between 0.08 and 0.20 AU. While some extra-solar planets are found at these radii, there is a relative dearth of planets between $\sim 0.06 - 0.6$ AU, and most close-in planets are “piled-up” near 0.03 – 0.04 AU (e.g., Udry et al. 2003). Thus, our measured inner dust disk sizes are larger than expected based on the exo-planet period distribution.

This discrepancy suggests that the gaseous components of disks extend further toward the star than the dust components, and that planetary migration halts in resonances with these gaseous truncation radii as argued by Lin et al. (1996). Gaseous material within the dust disk truncation radius is also consistent with the discrepancy between measured sizes and calculated magnetospheric radii discussed above. Assuming our inferred magnetospheric radii correspond to the inner edges of gaseous disks, we predict resonant orbits between 0.02 and 0.08 AU from the central star, compatible with the observed pile-up location for migrating exo-planets.

An alternate explanation for the apparent discrepancy between resonant orbits predicted by the dust truncation sizes and those actually observed is that the observed exo-planet period distribution is due to migration that occurred in an earlier evolutionary stage, when smaller disk truncation radii led to smaller resonant orbits. Observations of larger samples,

spanning a range of inner radii, are necessary to address this issue properly.

6. Conclusions

We have observed three $1 M_{\odot}$ T Tauri stars and one $2M_{\odot}$ T Tauri star with the Keck Interferometer to constrain the structure of the innermost regions of their circumstellar disks. High-resolution near-IR adaptive optics images, optical photometry, and optical spectra aided in the analysis of the interferometry data, and enabled us to estimate various properties of the systems, including mass accretion rates and co-rotation radii.

The main result of our analysis is that inner disks around solar-mass T Tauri stars appear similar to those around higher-mass T Tauri and Herbig Ae stars. Specifically, the observations for most sources are more consistent with puffed-up inner disk models than with geometrically flat accretion disk models.

We tested the theory of magnetospheric accretion by comparing our measured inner dust disk radii with calculated co-rotation and magnetospheric truncation radii. All measured sizes are larger than the magnetospheric and co-rotation radii. Moreover, the difference between measured sizes and inferred magnetospheric/co-rotation radii seems to increase with accretion rate: the discrepancy is small for AS 207A and V2508 Oph, but large for AS 205A and PX Vul. We suggest that accretional heating leads to dust sublimation at radii larger than R_{mag} . Since higher accretion rates cause larger sublimation radii but smaller magnetospheric radii, this hypothesis can explain our results. Thus, gaseous disks may extend inward to R_{mag} , while dust disks are truncated further out by sublimation.

Comparison of the observed inner disk sizes with the period distribution of extra-solar planets provides support for the hypothesis that gaseous disks extend further inward than dust disk truncation radii, since our measured inner disk sizes predict 2:1 resonances (which could halt migration) farther from the star than observed for extra-solar planets. In contrast, inferred magnetospheric radii predict resonant orbits that are compatible with the observed semi-major axis distribution of exo-planets.

Acknowledgments: The near-IR interferometry data presented in this paper were obtained with the Keck Interferometer (KI), which is supported by NASA. We wish to thank the entire KI team for making these observations possible. Observations were carried out at the W.M. Keck Observatory, which is operated as a scientific partnership among California Institute of Technology, the University of California, and NASA. The Observatory was made possible by the generous financial support of the W.M. Keck Foundation. The authors wish to recognize and acknowledge the cultural role and reverence that the summit of Mauna

Kea has always had within the indigenous Hawaiian community. We are most fortunate to have the opportunity to conduct observations from this mountain. This publication makes use of data products from the Two Micron All Sky Survey, which is a joint project of the University of Massachusetts and the Infrared Processing and Analysis Center, funded by the National Aeronautics and Space Administration and the National Science Foundation. 2MASS science data and information services were provided by the Infrared Science Archive at IPAC. This work has used software from the Michelson Science Center at the California Institute of Technology. J.A.E. acknowledges support from a Michelson Graduate Research Fellowship.

REFERENCES

- Adams, F. C., Lada, C. J., & Shu, F. H. 1988, *ApJ*, 326, 865
- Akeson, R. L., Ciardi, D. R., van Belle, G. T., Creech-Eakman, M. J., & Lada, E. A. 2000, *ApJ*, 543, 313
- Akeson, R. L., Walker, C. H., Wood, K., Eisner, J. A., Scire, E., Penprase, B., Ciardi, D. R., van Belle, G. T., Whitney, B., & Bjorkman, J. E. 2005, *ApJ*, in press
- Baraffe, I., Chabrier, G., Allard, F., & Hauschildt, P. H. 1998, *A&A*, 337, 403
- Barsony, M., Koresko, C., & Matthews, K. 2003, *ApJ*, 591, 1064
- Beckwith, S. V. W., Sargent, A. I., Chini, R. S., & Guesten, R. 1990, *AJ*, 99, 924
- Bertout, C., Basri, G., & Bouvier, J. 1988, *ApJ*, 330, 350
- Boden, A. F., Colavita, M. M., van Belle, G. T., & Shao, M. 1998, in *Proc. SPIE Vol. 3350*, p. 872-880, *Astronomical Interferometry*, Robert D. Reasenberg; Ed., 872-880
- Bouvier, J. 1990, *AJ*, 99, 946
- Calvet, N. & Gullbring, E. 1998, *ApJ*, 509, 802
- Chiang, E. I. & Goldreich, P. 1997, *ApJ*, 490, 368
- Chini, R. 1981, *A&A*, 99, 346
- Colavita, M., Akeson, R., Wizinowich, P., Shao, M., Acton, S., Beletic, J., Bell, J., Berlin, J., Boden, A., Booth, A., Boutell, R., Chaffee, F., Chan, D., Chock, J., Cohen, R., Crawford, S., Creech-Eakman, M., Eychaner, G., Felizardo, C., Gathright, J., Hardy,

- G., Henderson, H., Herstein, J., Hess, M., Hovland, E., Hrynevych, M., Johnson, R., Kelley, J., Kendrick, R., Koresko, C., Kurpis, P., Le Mignant, D., Lewis, H., Ligon, E., Lupton, W., McBride, D., Mennesson, B., Millan-Gabet, R., Monnier, J., Moore, J., Nance, C., Neyman, C., Niessner, A., Palmer, D., Reder, L., Rudeen, A., Saloga, T., Sargent, A., Serabyn, E., Smythe, R., Stomski, P., Summers, K., Swain, M., Swanson, P., Thompson, R., Tsubota, K., Tumminello, A., van Belle, G., Vasisht, G., Vause, J., Walker, J., Wallace, K., & Wehmeier, U. 2003, *ApJ*, 592, L83
- Colavita, M. M. 1999, *PASP*, 111, 111
- Colavita, M. M. & Wizinowich, P. L. 2003, in *Interferometry for Optical Astronomy II*. Edited by Wesley A. Traub. *Proceedings of the SPIE*, Volume 4838, pp. 79-88 (2003)., 79–88
- D’Alessio, P., Calvet, N., Hartmann, L., Lizano, S., & Cantó, J. 1999, *ApJ*, 527, 893
- D’Antona, F. & Mazzitelli, I. 1997, *Memorie della Societa Astronomica Italiana*, 68, 807
- Doppmann, G. W., Jaffe, D. T., & White, R. J. 2003, *AJ*, 126, 3043
- Draine, B. T. & Lee, H. M. 1984, *ApJ*, 285, 89
- Dullemond, C. P. & Dominik, C. 2004a, *A&A*, 417, 159
- . 2004b, *A&A*, 421, 1075
- Dullemond, C. P., Dominik, C., & Natta, A. 2001, *ApJ*, 560, 957
- Dutrey, A., Guilloteau, S., Duvert, G., Prato, L., Simon, M., Schuster, K., & Menard, F. 1996, *A&A*, 309, 493
- Edwards, S., Hartigan, P., Ghandour, L., & Andrulis, C. 1994, *AJ*, 108, 1056
- Eisner, J. A., Lane, B. F., Akeson, R. L., Hillenbrand, L., & Sargent, A. 2003, *ApJ*, 588, 360
- Eisner, J. A., Lane, B. F., Hillenbrand, L., Akeson, R., & Sargent, A. 2004, *ApJ*, 613, 1049
- Geoffray, H. & Monin, J.-L. 2001, *A&A*, 369, 239
- Ghez, A. M., Neugebauer, G., & Matthews, K. 1993, *AJ*, 106, 2005
- Ghosh, P. & Lamb, F. K. 1979a, *ApJ*, 232, 259
- . 1979b, *ApJ*, 234, 296
- Gullbring, E., Calvet, N., Muzerolle, J., & Hartmann, L. 2000, *ApJ*, 544, 927

- Gullbring, E., Hartmann, L., Briceno, C., & Calvet, N. 1998, *ApJ*, 492, 323
- Hartigan, P. & Kenyon, S. J. 2003, *ApJ*, 583, 334
- Hartmann, L. & Stauffer, J. R. 1989, *AJ*, 97, 873
- Hayashi, C. 1981, *Progress of Theoretical Physics*, 70, 35
- Hayward, T. L., Brandl, B., Pirger, B., Blacken, C., Gull, G. E., Schoenwald, J., & Houck, J. R. 2001, *PASP*, 113, 105
- Herbig, G. H. & Kameswara Rao, N. 1972, *ApJ*, 174, 401
- Herbst, W., Warner, J. W., Miller, D. P., & Herzog, A. 1982, *AJ*, 87, 98
- Hernández, J., Calvet, N., Briceño, C., Hartmann, L., & Berlind, P. 2004, *AJ*, 127, 1682
- Hillenbrand, L. A., Strom, S. E., Vrba, F. J., & Keene, J. 1992, *ApJ*, 397, 613
- Hillenbrand, L. A. & White, R. J. 2004, *ApJ*, 604, 741
- Jensen, E. L. N. & Mathieu, R. D. 1997, *AJ*, 114, 301
- Johns-Krull, C. M., Valenti, J. A., & Gafford, A. D. 2003, in *Revista Mexicana de Astronomia y Astrofisica Conference Series*, 38–44
- Kenyon, S. J., Yi, I., & Hartmann, L. 1996, *ApJ*, 462, 439
- Koerner, D. W. & Sargent, A. I. 1995, *AJ*, 109, 2138
- Königl, A. 1991, *ApJ*, 370, L39
- Koresko, C. D. 2002, *AJ*, 124, 1082
- Kuchner, M. J. & Lecar, M. 2002, *ApJ*, 574, L87
- Landolt, A. U. 1992, *AJ*, 104, 340
- Leinert, C., van Boekel, R., Waters, L. B. F. M., Chesneau, O., Malbet, F., Köhler, R., Jaffe, W., Ratzka, T., Dutrey, A., Preibisch, T., Graser, U., Bakker, E., Chagnon, G., Cotton, W. D., Dominik, C., Dullemond, C. P., Glazenborg-Kluttig, A. W., Glindemann, A., Henning, T., Hofmann, K.-H., de Jong, J., Lenzen, R., Ligi, S., Lopez, B., Meisner, J., Morel, S., Paresce, F., Pel, J.-W., Percheron, I., Perrin, G., Przygodda, F., Richichi, A., Schöller, M., Schuller, P., Stecklum, B., van den Ancker, M. E., von der Lühe, O., & Weigelt, G. 2004, *A&A*, 423, 537

- Lin, D. N. C., Bodenheimer, P., & Richardson, D. C. 1996, *Nature*, 380, 606
- Lynden-Bell, D. & Pringle, J. E. 1974, *MNRAS*, 168, 603
- Malbet, F., Berger, J.-P., Colavita, M. M., Koresko, C. D., Beichman, C., Boden, A. F., Kulkarni, S. R., Lane, B. F., Mobley, D. W., Pan, X. P., Shao, M., van Belle, G. T., & Wallace, J. K. 1998, *ApJ*, 507, L149
- Malbet, F., Lachaume, R., Berger, J.-P., Colavita, M. M., Di Folco, E., Eisner, J. A., Lane, B. F., Millan-Gabet, R., Ségransan, D., & Traub, W. 2005, *A&A*, submitted
- Marcy, G. W. & Butler, R. P. 2000, *PASP*, 112, 137
- McCaughrean, M. J. & O'Dell, C. R. 1996, *AJ*, 111, 1977
- Merrill, P. W. & Burwell, C. G. 1950, *ApJ*, 112, 72
- Millan-Gabet, R., Schloerb, F. P., & Traub, W. A. 2001, *ApJ*, 546, 358
- Millan-Gabet, R., Schloerb, F. P., Traub, W. A., Malbet, F., Berger, J. P., & Bregman, J. D. 1999, *ApJ*, 513, L131
- Monnier, J. D. & Millan-Gabet, R. 2002, *ApJ*, 579, 694
- Mora, A., Merín, B., Solano, E., Montesinos, B., de Winter, D., Eiroa, C., Ferlet, R., Grady, C. A., Davies, J. K., Miranda, L. F., Oudmaijer, R. D., Palacios, J., Quirrenbach, A., Harris, A. W., Rauer, H., Cameron, A., Deeg, H. J., Garzón, F., Penny, A., Schneider, J., Tsapras, Y., & Wesselius, P. R. 2001, *A&A*, 378, 116
- Muzerolle, J., Calvet, N., Hartmann, L., & D'Alessio, P. 2003, *ApJ*, 597, L865
- Piorno Schiavon, R., Batalha, C., & Barbuy, B. 1995, *A&A*, 301, 840
- Pollack, J. B., Hollenbach, D., Beckwith, S., Simonelli, D. P., Roush, T., & Fong, W. 1994, *ApJ*, 421, 615
- Prato, L., Greene, T. P., & Simon, M. 2003, *ApJ*, 584, 853
- Raymond, S. N., Quinn, T., & Lunine, J. I. 2004, *Icarus*, 168, 1
- Reipurth, B. & Zinnecker, H. 1993, *A&A*, 278, 81
- Salpeter, E. E. 1977, *ARA&A*, 15, 267
- Sasselov, D. D. & Lecar, M. 2000, *ApJ*, 528, 995

- Shevchenko, V. S. & Herbst, W. 1998, *AJ*, 116, 1419
- Shu, F., Najita, J., Ostriker, E., Wilkin, F., Ruden, S., & Lizano, S. 1994, *ApJ*, 429, 781
- Shu, F. H., Shang, H., Glassgold, A. E., & Lee, T. 1997, *Science*, 277, 1475
- Siess, L., Dufour, E., & Forestini, M. 2000, *A&A*, 358, 593
- Skrutskie, M. F., Meyer, M. R., Whalen, D., & Hamilton, C. 1996, *AJ*, 112, 2168
- Steenman, H. & Thé, P. S. 1991, *Ap&SS*, 184, 9
- Struve, O. & Rudkjøbing, M. 1949, *ApJ*, 109, 92
- Troy, M., Dekany, R. G., Brack, G., Oppenheimer, B. R., Bloemhof, E. E., Trinh, T., Dekens, F. G., Shi, F., Hayward, T. L., & Brandl, B. 2000, in *Proc. SPIE Vol. 4007*, p. 31-40, *Adaptive Optical Systems Technology*, Peter L. Wizinowich; Ed., 31–40
- Udry, S., Mayor, M., & Santos, N. C. 2003, *A&A*, 407, 369
- Vogt, S. S., Allen, S. L., Bigelow, B. C., Bresee, L., Brown, B., Cantrall, T., Conrad, A., Couture, M., Delaney, C., Epps, H. W., Hilyard, D., Hilyard, D. F., Horn, E., Jern, N., Kanto, D., Keane, M. J., Kibrick, R. I., Lewis, J. W., Osborne, J., Pardeilhan, G. H., Pfister, T., Ricketts, T., Robinson, L. B., Stover, R. J., Tucker, D., Ward, J., & Wei, M. Z. 1994, in *Proc. SPIE Instrumentation in Astronomy VIII*, David L. Crawford; Eric R. Craine; Eds., Volume 2198, p. 362
- Walker, M. F. 1972, *ApJ*, 175, 89
- Walter, F. M. 1986, *ApJ*, 306, 573
- Weaver, W. B. & Jones, G. 1992, *ApJS*, 78, 239
- White, R. J. & Basri, G. 2003, *ApJ*, 582, 1109
- White, R. J. & Hillenbrand. 2004, *ApJ*, in press

A. The Spectroscopic Binary AS 205B

The Keck/HIRES spectrum of AS 205B (Figure 7; §2.5) showed it to be a double-lined spectroscopic binary, making AS 205 a hierarchical triple. Since the components of AS 205B, labeled Ba and Bb, are of similar brightness, slowly rotating, and reasonably well separated in velocity, their properties can be determined somewhat independently. We use a technique similar to that described in §3.1.1, but tailored to fit the components of a spectroscopic binary.

Radial velocities, rotational velocities, spectral types, and continuum excesses for the components of AS 205B are determined from the optical spectra. Radial velocities and $v \sin i$ values are estimated by fitting the two peaks of the cross-correlation function. AS 205Ba and Bb have radial velocities of $-0.30 \pm 0.46 \text{ km s}^{-1}$ and $-17.71 \pm 1.11 \text{ km s}^{-1}$, respectively. Both have projected rotational velocities below our measurement limits ($v \sin i_{Ba} \leq 5.9 \text{ km s}^{-1}$, $v \sin i_{Bb} \leq 10.2 \text{ km s}^{-1}$); the larger limit for AS 205Bb is a consequence of its fainter features. The flux ratio of the components, their spectral types, and the continuum excess of the system (defined here as $r = F_{excess}/(F_{Ba} + F_{Bb})$) are determined simultaneously by comparisons with synthetic spectroscopic binaries, generated by combining dwarf standards at the appropriate velocities. The best fit is determined by minimizing the root-mean-squared difference between AS 205B and the synthetic binary spectra over several temperature-sensitive regions. The components have spectral types of $K7 \pm 1$ (AS 205Ba) and $M0 \pm 1$ (AS 205Bb), and AS 205Ba is slightly brighter ($[F_{Ba}/F_{Bb}]_R = 1.52 \pm 0.12$, $[F_{Ba}/F_{Bb}]_I = 1.38 \pm 0.11$). The optical veiling of the system ($r_R = 0.83 \pm 0.12$, $r_I = 0.60 \pm 0.09$) suggests on-going accretion, although it is not possible to determine if this is onto the primary, the secondary or both. A high accretion rate is also consistent with the strong and broad $H\alpha$ emission (EW = -42.6 \AA ; 10% width = 384 km s^{-1}).

We estimate the visual extinction and luminosity of each component using the relative fluxes of the spectroscopic binary components at R and I in combination with spectral types, veiling, and the total AS 205B fluxes determined in §3.1.1. We determine visual extinctions of 3.9 mag and 3.4 mag, and luminosities of $0.44 L_{\odot}$ and $0.26 L_{\odot}$ for AS 205Ba and Bb, respectively. Comparison of the effective temperatures (4000 K, 3800 K) and luminosities with the Siess et al. (2000) pre-main sequence evolutionary models yields stellar masses of $0.74 M_{\odot}$ and $0.54 M_{\odot}$ and ages of 5.1 Myr and 5.4 Myr for AS 205Ba and Bb, respectively. Given the uncertainties, all three components of the AS 205 system appear to be coeval.

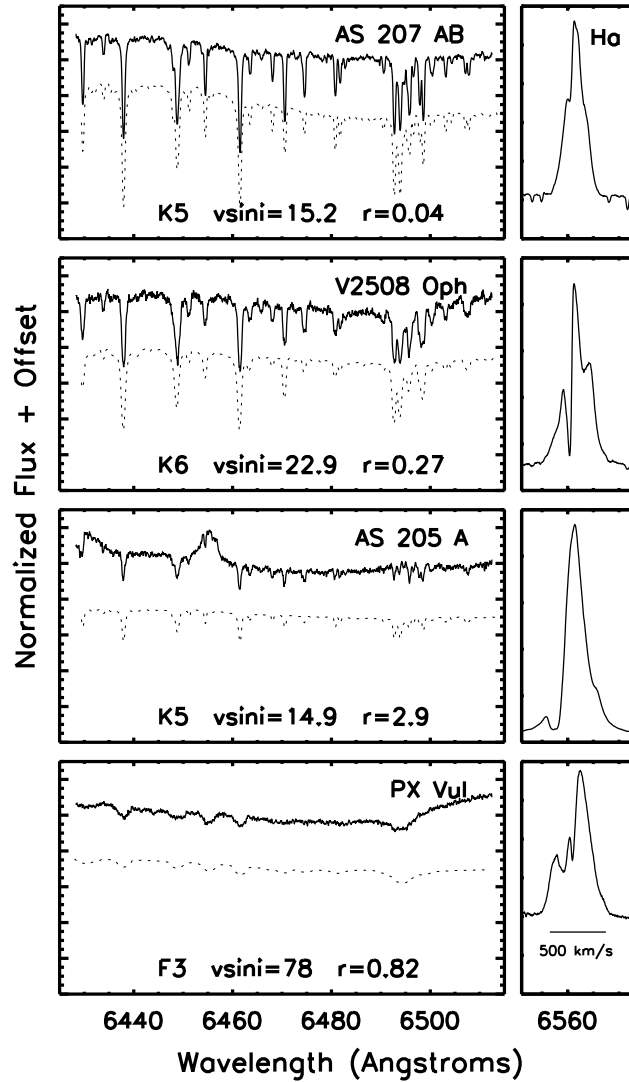


Fig. 1.— Portions of the Keck/HIRES spectra within the R-band (left), and H α emission profiles (right); both panels have the same wavelength scale. The best fit dwarf standards, rotationally broadened and optically veiled, are shown as dashed lines for comparison. The strong, broad H α emission profiles suggest all stars are accreting.

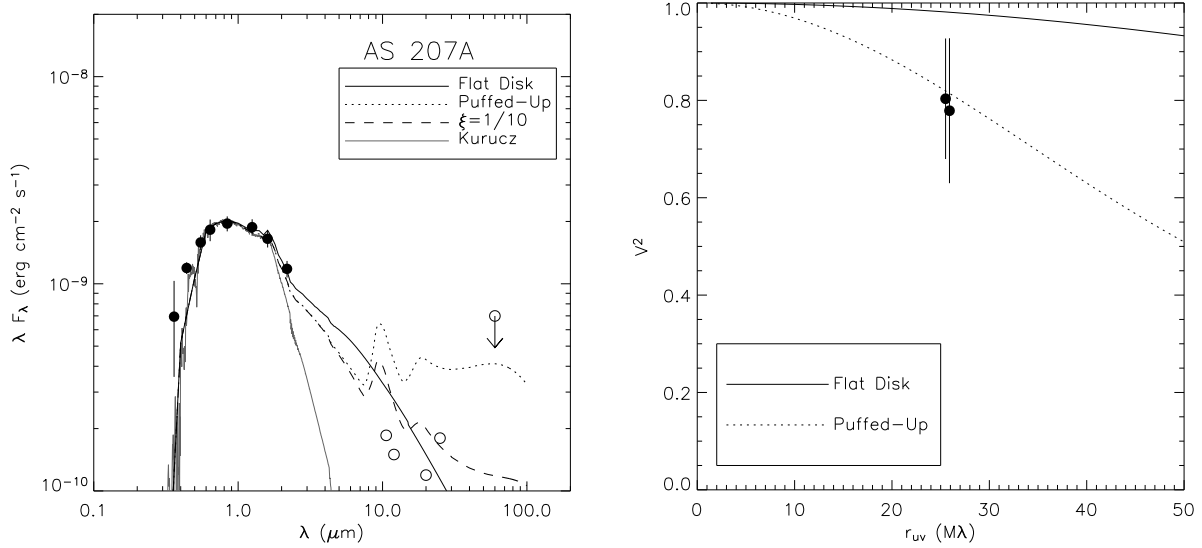


Fig. 2.— (left) Reddening-corrected fluxes for AS 207A from optical through near-IR wavelengths (filled circles), supplemented with longer-wavelength fluxes from the literature (open circles; Weaver & Jones 1992; Jensen & Mathieu 1997; Prato et al. 2003; Koresko 2002). Predicted SEDs for geometrically flat accretion disks (solid black line), and flared disks with puffed-up inner rims (dotted line), as well as the Kurucz model atmosphere with the stellar parameters determined in §3.1.1 (solid gray line), are also plotted. Only *RIJK* photometry, probing the star and inner disk, was used in the fits. We also plot the SED predicted by a flared disk model with an intermediate flaring index, $\xi = 1/10$ (dashed line). (right) Squared visibilities measured with KI, as a function of *uv* radius, along with the predictions of different models. The two curves are labeled as in the left panel: the solid black line indicates the model determined by fitting a flat accretion disk to the V^2 +SED dataset, and the dotted line represents the V^2 for the best-fit puffed-up inner disk wall model. For AS 207A, the puffed-up inner disk model provides a superior fit to the data. The long-wavelength photometry is compatible with an un-flared outer disk.

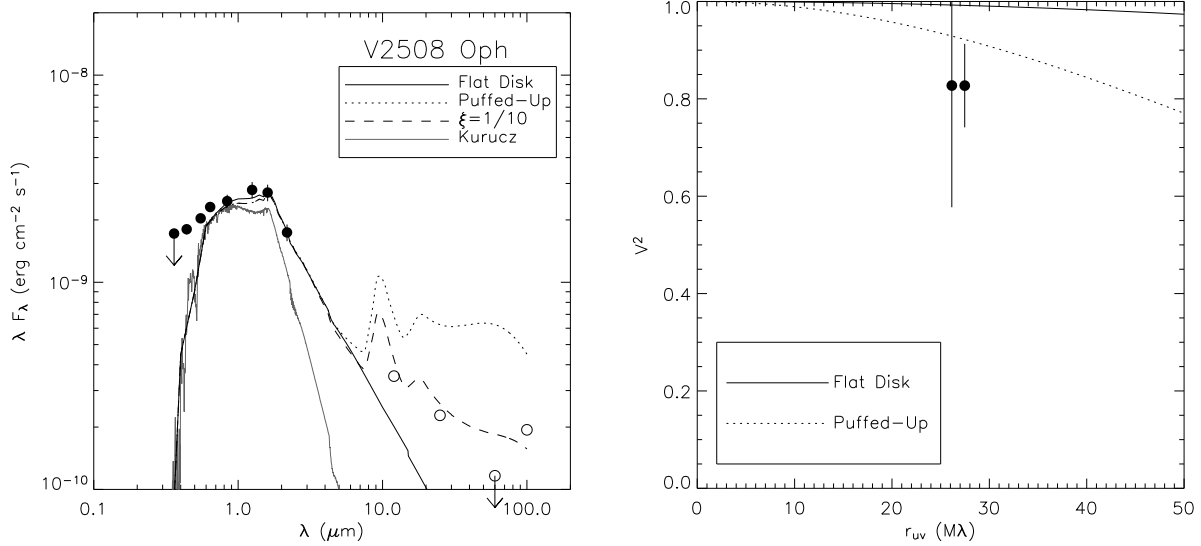


Fig. 3.— SEDs and squared visibilities for V2508 Oph, labeled as in Figure 2. For this source, the puffed-up inner disk model provides a superior fit to the SED and V^2 data. The IRAS photometry for this source is more consistent with a moderately flared disk model (with $\xi \sim 1/10$) than with a flat disk model.

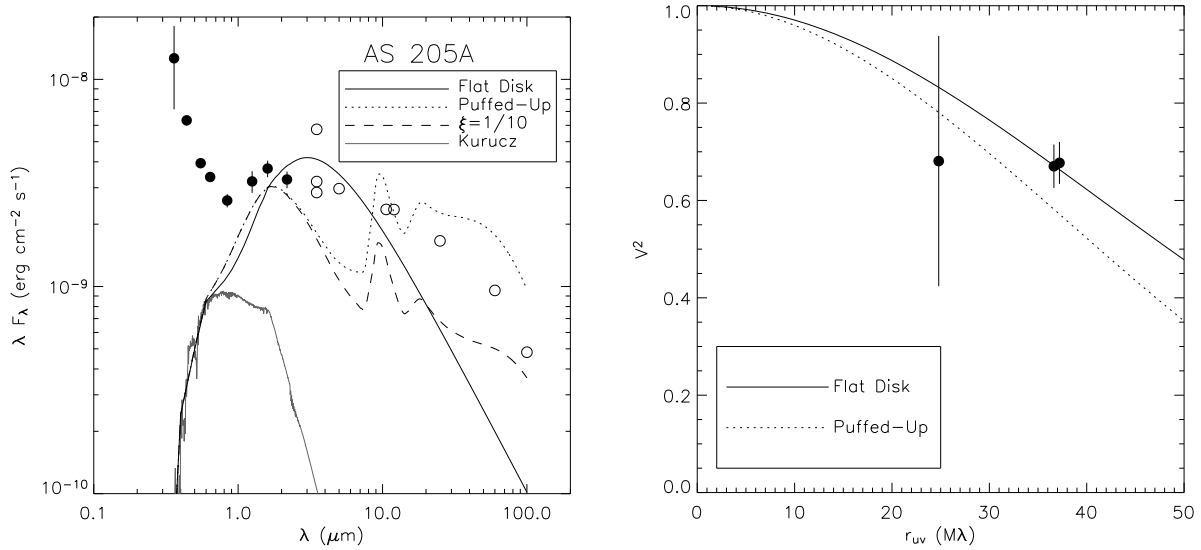


Fig. 4.— SEDs and squared visibilities for AS 205A, labeled as in Figure 2. For this source, the flat disk model provides a better fit than the puffed up inner disk model to the SED and V^2 data, although neither model fits very well. These poor fits are likely due to near-IR emission from hot accretion shocks that is not accounted for in our models. The fact that the long-wavelength photometry lies above the model predictions suggests that flaring and accretion heating are important in the outer disk.

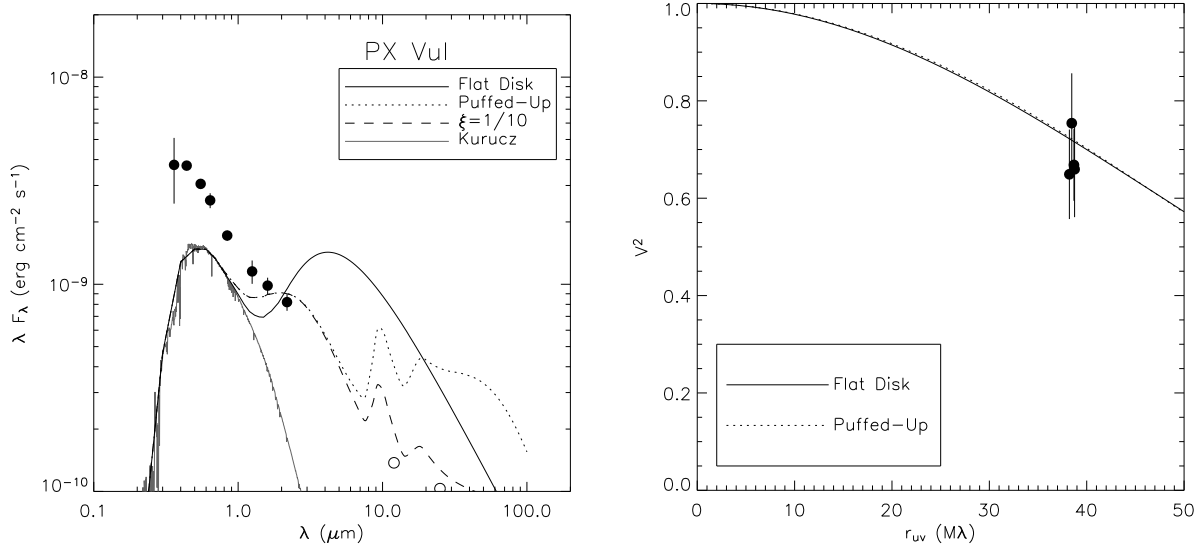


Fig. 5.— SEDs and squared visibilities for PX Vul, labeled as in Figure 2. For this source, the puffed-up inner disk model provides a superior fit to the SED and V^2 data. The long-wavelength photometry is compatible with an un-flared outer disk. Note that for this object, both models fit the V^2 data, but lead to significant deviations in the near-IR SEDs, while for other sources, the SEDs are similar but the V^2 predictions differ (Figures 2–4); this is due to the fact that we have more V^2 measurements for PX Vul, and the combined V^2 +SED fits are therefore dominated by the interferometric rather than the photometric data.

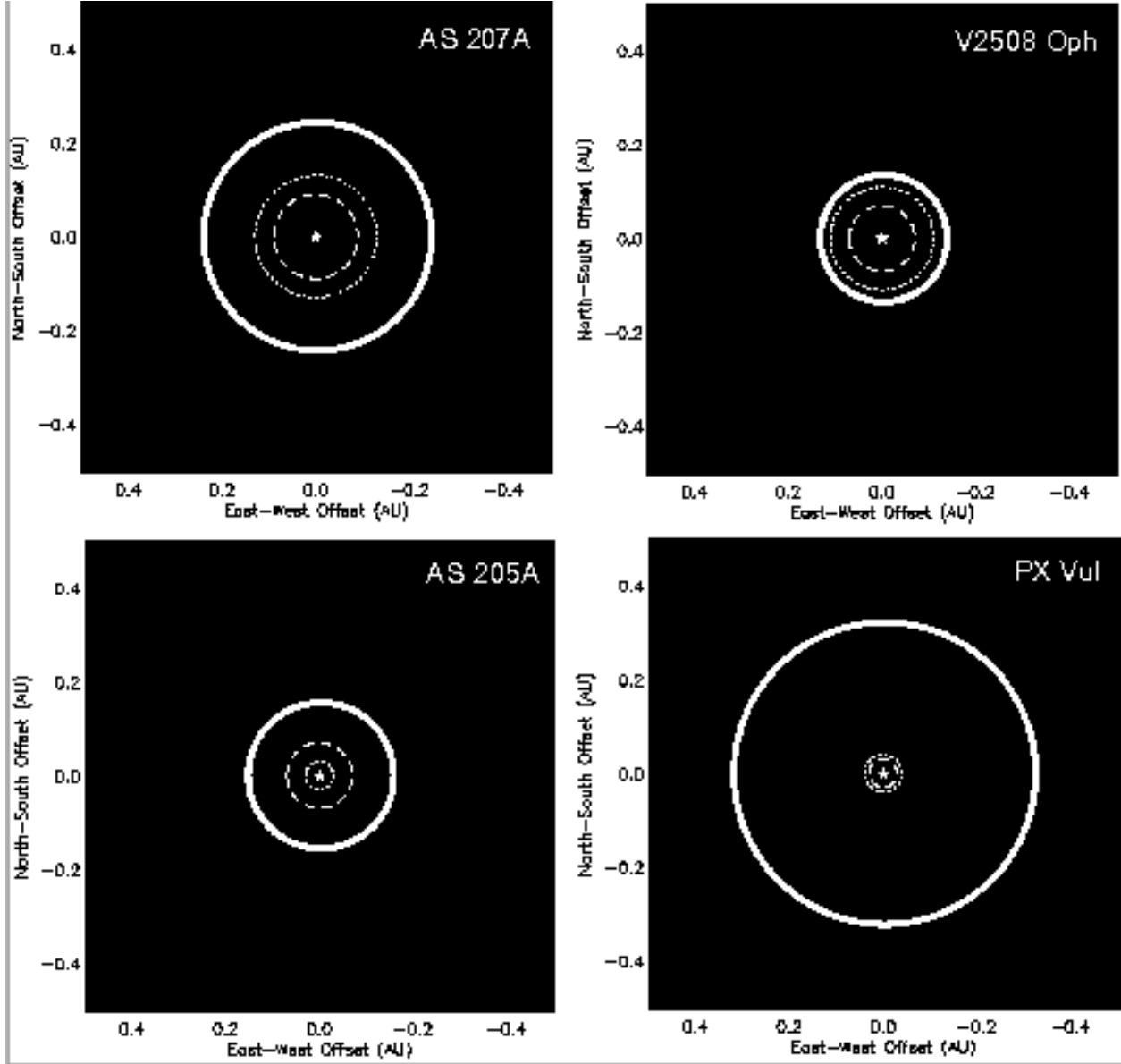


Fig. 6.— Images of the best-fit puffed-up inner disk models for our sample, with inner sizes and temperatures given in Table 5. Because the puffed-up inner rims dominate the $2.2 \mu\text{m}$ emission, the images appear ring-like. The magnetospheric truncation radii and (limits on) co-rotation radii (Table 4) are indicated by dotted and dashed lines, respectively. For AS 205A, V2508 Oph, and PX Vul, the plotted co-rotation radii are upper limits. The positions of the central stars are indicated with symbols.

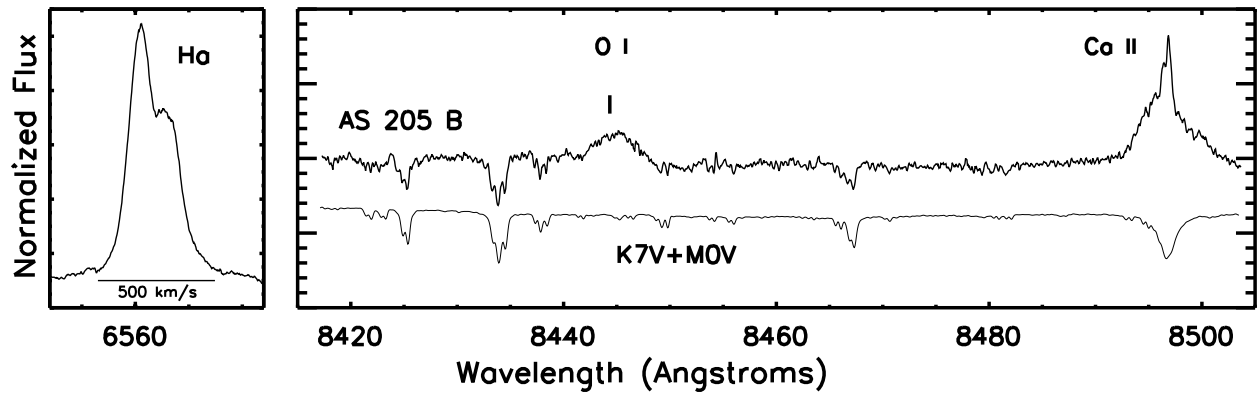


Fig. 7.— Portions of the Keck/HIRES spectrum of the double-lined spectroscopic binary AS 205B at H α and within the *I*-band; both panels have the same wavelength scale. The strong, broad H α , O I 8446 Å, and Ca II 8496 Å emission features suggest on-going accretion. The photospheric features are best matched by combining K7 and M0 dwarfs plus an optical excess (see Appendix A).

Table 1. Observed Properties of Sample

Source	Alt. Name	α (J2000)	δ (J2000)	d (pc)	SpTy	r_R	r_I	$v \sin i$ (km s ⁻¹)	v_{helio} (km s ⁻¹)	EW	H α 10% width
AS 207A	SR 9	16 27 40.28	-24 22 04.0	160 ^a	K5 \pm 1	0.04 \pm 0.07	-0.07 \pm 0.15	15.2 \pm 0.9	-7.17 \pm 0.25	-16.4	342
V2508 Oph	Oph 6	16 48 45.62	-14 16 35.9	160 ^a	K6 \pm 1	0.27 \pm 0.07	0.09 \pm 0.10	22.9 \pm 1.0	-8.26 \pm 0.56	-32.5	278
AS 205A	V866 Sco	16 11 31.40	-18 38 24.5	160 ^a	K5 \pm 1	2.94 \pm 0.32	1.95 \pm 0.20	14.9 \pm 1.8	-11.60 \pm 0.87	-99.6	388
PX Vul	LkH α 483-41	19 26 40.30	+23 53 49.0	420 ^b	F3 \pm 2 ^{c,d}	0.82 \pm 0.39	0.62 \pm 0.45	78 \pm 11	-7.0 \pm 2.5	-9.4	512

References. — Spectral types, veilings (ratios of excess to stellar flux) at R and I bands, $v \sin i$ values, heliocentric radial velocities, H α equivalent widths, and H α widths at 10% of the peak, are determined from high-resolution optical spectroscopy (§2.5). a —Chini (1981); b —Herbst et al. (1982); c —Mora et al. (2001); d —Hernández et al. (2004). Distance estimates are likely uncertain by 10-20%.

Table 2. Photometry of Observed Sources

Source	U	B	V	R	I	J	H	K
AS 207A ^a	13.52 ± 0.53	13.00 ± 0.07	11.78 ± 0.09	10.95 ± 0.13	9.80 ± 0.09	8.69 ± 0.05	7.96 ± 0.06	7.31 ± 0.06
V2508 Oph	15.74 ± 1.35	15.04 ± 0.06	13.45 ± 0.03	12.29 ± 0.04	10.74 ± 0.08	8.75 ± 0.04	7.73 ± 0.07	7.04 ± 0.08
AS 205A ^a	13.69 ± 0.47	13.74 ± 0.06	12.76 ± 0.03	11.82 ± 0.04	10.52 ± 0.08	8.63 ± 0.13	7.41 ± 0.07	6.36 ± 0.08
PX Vul	12.42 ± 0.38	12.35 ± 0.05	11.55 ± 0.02	11.01 ± 0.09	10.32 ± 0.06	9.33 ± 0.14	8.59 ± 0.09	7.74 ± 0.10

References. — *a*—For AS 207A and AS 205A, which have known companions, the *UBVRI* photometry contains contributions from both components, while the *JHK* photometry reflects only the emission from the primaries.

Table 3. Binaries

Source	Sep ($''$)	$P.A.$ ($^\circ$)	ΔJ (mag)	ΔH (mag)	ΔK (mag)
AS 207B	0.63	354	1.59 ± 0.07	1.79 ± 0.09	2.19 ± 0.09
AS 205B ^a	1.31	213	1.10 ± 0.21	0.94 ± 0.10	0.91 ± 0.12

References. — *a*—AS 205B is a spectroscopic binary. See Appendix A for details.

Table 4. Inferred Stellar and Accretion Properties

Source	T_* (K)	L_* (L_\odot)	R_* (R_\odot)	A_v (mag)	M_* (M_\odot)	τ_* (Myr)	L_{acc} (L_\odot)	\dot{M} ($M_\odot \text{ yr}^{-1}$)	R_{mag} (AU)	R_{corot} (AU)	$F_{*,K}$ (Jy)	$F_{D,K}$ (Jy)
AS 207A	4400	2.7	2.9	1.6	1.2	1.1	0.4	3.2×10^{-8}	0.13	0.09	0.59	0.27
V2508 Oph	4200	3.3	3.5	3.5	0.9	0.6	1.6	2.3×10^{-7}	0.11	≤ 0.07	0.82	0.45
AS 205A	4400	1.3	2.0	3.6	1.2	3.2	13.0	7.2×10^{-7}	0.03	≤ 0.07	0.27	2.12
PX Vul	6600	13.7	2.9	2.0	1.9	6.9	25.0	1.3×10^{-6}	0.04	≤ 0.03	0.13	0.46

References. — Stellar parameters, accretion luminosities and rates, and magnetospheric and co-rotation radii determined using high-resolution optical spectra and *UBVRI* photometry (§3.1). Stellar and disk fluxes at $2.2 \mu\text{m}$ ($F_{*,K}$, $F_{D,K}$) determined using Kurucz models (with measured T_* , R_* , and adopted distances from Table 1) and de-reddened observed photometry (§3.2). As discussed in §3.1, we estimate that T_* is uncertain by ± 100 K, L_* , R_* , A_v , R_{mag} , and R_{corot} are uncertain by $\sim 30\%$, L_{acc} and \dot{M} are uncertain by a factor of 2-3, and $F_{*,K}$ and $F_{D,K}$ have error bars of $\sim 30 - 50\%$. The uncertainties on M_* and τ_* are more difficult to ascertain since they depend on pre-main sequence evolutionary models; however, we estimate that the relative uncertainties for these parameters are $\sim 30 - 50\%$.

Table 5. Disk Parameters from Near-IR Interferometry and SEDs

Source	χ_r^2	Flat Disks		Flared, Puffed-Up Disks		
		R_{in} (AU)	T_{in} (K)	χ_r^2	R_{in} (AU)	T_{in} (K)
Combined V^2 +SED Results						
AS 207A	1.070	$0.04^{+0.01}_{-0.02}$	1500^{+300}_{-100}	0.208	$0.23^{+0.11}_{-0.10}$	1000^{+200}_{-100}
V2508 Oph	1.409	$0.02^{+0.17}_{-0.01}$	2400^{+100}_{-1300}	0.981	$0.12^{+0.10}_{-0.10}$	1500^{+900}_{-300}
AS 205A	3.729	$0.07^{+0.01}_{-0.01}$	1900^{+100}_{-100}	6.072	$0.14^{+0.01}_{-0.01}$	1900^{+100}_{-100}
PX Vul	3.049	$0.22^{+0.01}_{-0.03}$	1400^{+100}_{-100}	1.072	$0.32^{+0.01}_{-0.04}$	1500^{+100}_{-100}
V^2 -only Results						
AS 207A	0.010	$0.17^{+0.04}_{-0.05}$	1500	0.010	$0.25^{+0.06}_{-0.07}$	1000
V2508 Oph	0.003	$0.10^{+0.04}_{-0.03}$	2400	0.003	$0.20^{+0.04}_{-0.13}$	1500
AS 205A	0.211	$0.07^{+0.01}_{-0.01}$	1900	0.224	$0.13^{+0.01}_{-0.01}$	1900
PX Vul	0.234	$0.23^{+0.01}_{-0.01}$	1400	0.234	$0.34^{+0.03}_{-0.02}$	1500
SED-only Results						
AS 207A	0.473	$0.04^{+0.01}_{-0.02}$	1500^{+300}_{-100}	0.327	$0.23^{+0.11}_{-0.23}$	1000^{+300}_{-100}
V2508 Oph	0.969	$0.02^{+0.03}_{-0.01}$	2400^{+100}_{-800}	0.870	$0.07^{+0.08}_{-0.07}$	1900^{+600}_{-500}
AS 205A	6.851	$0.06^{+0.01}_{-0.01}$	2000^{+200}_{-100}	4.796	$0.23^{+0.01}_{-0.03}$	1600^{+100}_{-100}
PX Vul	1.341	$0.05^{+0.03}_{-0.01}$	2400^{+100}_{-400}	0.842	$0.21^{+0.06}_{-0.04}$	1800^{+200}_{-200}

References. — Columns 2-4 list the reduced χ^2 values, inner radii, and inner temperatures for best-fit flat accretion disk models. Columns 5-7 list χ_r^2 , R_{in} , and T_{in} for best-fit puffed-up inner disk models. Results are shown for fits to combined V^2 +SED datasets as well as V^2 and SEDs individually. For the V^2 -only fits, we assumed the best-fit temperature from the combined V^2 +SED analysis, fitting only for R_{in} .

Table 6. Measured versus Predicted Inner Disk Sizes

Source	Flat Disks			Flared, Puffed-Up Disks		
	$R_{\text{in,meas}}$ (AU)	$R_{\text{in},\dot{M}=0}$ (AU)	$R_{\text{in},\dot{M}\neq 0}$ (AU)	$R_{\text{in,meas}}$ (AU)	$R_{\text{in},\dot{M}=0}$ (AU)	$R_{\text{in},\dot{M}\neq 0}$ (AU)
AS 207A	$0.17^{+0.04}_{-0.05}$	0.03	0.04	$0.23^{+0.11}_{-0.10}$	0.26	0.28
V2508 Oph	$0.10^{+0.04}_{-0.03}$	0.02	0.03	$0.12^{+0.10}_{-0.10}$	0.13	0.16
AS 205A	$0.07^{+0.01}_{-0.01}$	0.01	0.07	$0.14^{+0.01}_{-0.01}$	0.05	0.17
PX Vul	$0.23^{+0.01}_{-0.01}$	0.06	0.15	$0.32^{+0.01}_{-0.04}$	0.27	0.46

References. — Measured sizes ($R_{\text{in,meas}}$) taken from Table 5, compared to expectations for disk models based on inferred inner disk temperatures and stellar parameters. For the puffed-up inner disk models, we use the sizes measured from combined V^2 +SED analysis, while for the flat disk models, where models generally provide poor fits to the V^2 and SED values simultaneously, we use measured sizes from V^2 -only analysis. Expected inner disk sizes for the flat and puffed-up disk models are calculated from Equations 7–8, assuming no accretion ($R_{\text{in},\dot{M}=0}$) and using the inferred accretion rates from Table 1 ($R_{\text{in},\dot{M}\neq 0}$).